

## **Synthesis of Bioactive Glass Doped With Bismuth, Zinc, and Copper for Bone Regeneration: Structural and Hemodynamic Analysis Employing ANSYS Static Structural and Fluent Modeling**

ADRI, Anindita, ZAHID, Nayeem Bin, HOSSAIN, Nazmul, HOSSAIN, Md Sahadath, AHMED, Samina, ARAFAT, Abul and SAMAD, Sabrin A  
<<http://orcid.org/0000-0001-7385-2480>>

Available from Sheffield Hallam University Research Archive (SHURA) at:

<https://shura.shu.ac.uk/36590/>

---

This document is the Published Version [VoR]

### **Citation:**

ADRI, Anindita, ZAHID, Nayeem Bin, HOSSAIN, Nazmul, HOSSAIN, Md Sahadath, AHMED, Samina, ARAFAT, Abul and SAMAD, Sabrin A (2025). Synthesis of Bioactive Glass Doped With Bismuth, Zinc, and Copper for Bone Regeneration: Structural and Hemodynamic Analysis Employing ANSYS Static Structural and Fluent Modeling. Nano Select. [Article]

---


### **Copyright and re-use policy**

See <http://shura.shu.ac.uk/information.html>



## RESEARCH ARTICLE OPEN ACCESS

# Synthesis of Bioactive Glass Doped With Bismuth, Zinc, and Copper for Bone Regeneration: Structural and Hemodynamic Analysis Employing ANSYS Static Structural and Fluent Modeling

Anindita Adri<sup>1</sup> | Nayeem Bin Zahid<sup>1</sup> | Nazmul Hossain<sup>1</sup> | Md Sahadath Hossain<sup>2</sup> | Samina Ahmed<sup>2</sup> | Abul Arafat<sup>3</sup> | Sabrin A. Samad<sup>1</sup> 

<sup>1</sup>Department of Nuclear Engineering, University of Dhaka, Dhaka, Bangladesh | <sup>2</sup>Institute of Glass and Ceramic Research & Testing, Bangladesh Council of Scientific and Industrial Research (BCSIR), Dhaka, Bangladesh | <sup>3</sup>Additive Manufacturing of Functional Materials Research Group, Centre For Engineering Innovation and Research, University of Wolverhampton, Telford Innovation Campus, Telford, UK

**Correspondence:** Sabrin A. Samad ([sabrinsamad@du.ac.bd](mailto:sabrinsamad@du.ac.bd))

**Received:** 25 June 2025 | **Revised:** 19 September 2025 | **Accepted:** 3 November 2025

**Keywords:** ANSYS structural analysis | bioactive glass | computational fluid dynamics | radioisotopes

## ABSTRACT

Bioactive glasses (BG) are heavily explored biomaterials especially for their bone and tissue regenerative property and biocompatibility. In this study, the synthesis of BG doped with Bi, Zn, and Cu (representative of Bi-213, Cu-64, and Zn-65 radioisotopes) was investigated at 100°C via the sol-gel method, followed by calcination at 700°C. Addition of dopants such as Bi, Zn, and Cu enhance the localized treatment of bone malignancies, aiming to combine therapeutic effects with enhanced mechanical integrity. The composition of the BG consisted roughly of 50% SiO<sub>2</sub>, 25% Na<sub>2</sub>O, and 25% CaO. X-ray diffraction (XRD) and Fourier transform infrared spectroscopy (FTIR) were used to identify the crystalline phases and to determine the presence of specific functional groups in the BG, respectively. The XRD peaks demonstrated that Sodium Calcium Silicate (Devitrite) was present in the synthesized BG where highest intensity peak was observed at  $2\theta = 29.8^\circ$ . A finite element analysis (FEA) was performed on the scaffold model with undoped BG properties to investigate the effect of blood pressure, which revealed minimal overall deformation averaging  $\sim 0.12 \text{ \AA}$ , with edge deformation ranging from 1.58 to 0.635  $\text{\AA}$ . Furthermore, CFD analyses were conducted to explore the flow distribution through the microchannel network of the scaffold, which indicated favorable blood flow and pressure distribution throughout the BG.

## 1 | Introduction

Bioactive glass (BG) is a type of glass-ceramic biomaterials widely recognized for their ability to regenerate damaged bones and support in the repairment process. These materials are predominantly composed of silicate networks, capable of releasing

therapeutic ions upon interaction with body fluids, thereby initiating a cascade of biological responses suitable for bone healing [1]. For non-load bearing bone defects, an effective scaffold must replicate the three-dimensional fibrous architecture of the extracellular matrix (ECM), providing a conducive environment for cell attachment, proliferation, and differentiation [2].

**Abbreviations:** BG, bioactive glass; CFD, computational fluid dynamics; FTIR, Fourier transform infrared spectroscopy; XRD, X-ray diffraction.

This is an open access article under the terms of the [Creative Commons Attribution](https://creativecommons.org/licenses/by/4.0/) License, which permits use, distribution and reproduction in any medium, provided the original work is properly cited.

© 2025 The Author(s). *Nano Select* published by Wiley-VCH GmbH.



The field of bioactive glass has observed substantial evolution since the pioneering of L. Hench, who introduced the high-temperature melt-quenching technique in 1969. Although the melt quenching process enhances mechanical strength and structural uniformity, it may result in phase separation, which can form unwanted crystalline phases and reduced bioactivity. Later on, in 1991, Li et al. introduced the sol-gel technique, which enabled low temperature synthesis ranging from 600°C to 700°C, while preserving the bioactivity of the resulting material [3]. Various adaptations of the sol-gel method have emerged since then. For instance, Charlena et al. synthesized fluorapatite from snail shells (*Achatina fulica*) using the sol-gel technique and concluded that optimal crystallinity was obtained at 900°C [4]. In parallel, Jianhang Du et al. employed bismuth coating on a 3D-printed bioactive glass scaffolds to serve as a photothermal anticancer therapy while promoting bone regeneration [5]. Further investigations into compositional tuning have underscored the benefits of incorporating various metal oxides. For example, Kenawy et al. developed nano-sized bismuth oxide and iron oxide based bioglass using sol-gel [6]. The cell culture experiments demonstrated that MC3T3-E1 cells showed enhanced osteoblastic cell adhesion, particularly in iron oxide-incorporated variants. Similarly, M. M. Farag et al. studied substitution of SrO for Na<sub>2</sub>O in 45S5 bioactive glass resulting in reduced toxicity and improved antibacterial and osteogenic performance. Enhancements were further achieved via gamma irradiation, which increased glass dissolution and promoted fibroblast proliferation, suggesting promising clinical applications [7].

Regarding fabrication, new methods are still evolving that enhances the accuracy and scalability of BG synthesis. Michał Wojasinski and Joanna Latocha made advancements in fabrication techniques by presenting a novel 3D-printed BOX reactor to facilitate the production of nHAp at a larger scale and further demonstrated improved hydrodynamic conditions found in single-channel milli reactors [8]. The investigation was significantly influenced by the 3D-printed BOX modeled by Michał and Joanna et al. and an identical box was attempted to design in *SpaceClaim*, in order to circulate blood across the bioglass scaffold. Similarly, Elena Marcello et al. constructed reproducible 3D P(3HO-co-3HD-co-3HDD) scaffolds, showing 100% high cell viability toward the MC3T3-E1 cells [9]. Complementing these structural innovations, computational studies by Cortes Williams III have revealed that pore size distribution in scaffolds, particularly smaller pores in the upper layers, can significantly affect shear stress levels, thereby influencing nutrient flow and cell proliferation [10]. These findings justify the integration of computational modeling into material design, enabling predictive evaluations of scaffold behavior under physiological conditions.

Built on these foundational studies, the present work investigates doping of radioactive Bi, Zn, and Cu in bioactive glasses. The inclusion of radioactive isotopes such as Bi-213 (derived from Ac-225) [9], Cu-64, Cu-67, and Zn-65 offer varied biological half-lives and therapeutic windows which are targeted for radiotherapeutic applications. Bi-213, specifically affects nearby tissues while avoiding healthy ones from damage. On the other hand, Cu-64 and Cu-67, with half-lives of 12.7 [11] and 61.83 h respectively, support both diagnostic and therapeutic roles. Zinc-65, with a significantly longer half-life of 244 days [12], contributes to

sustained antibacterial action. The presence of Cu and Zn ions enhances osteogenic activity and reduces infection risk, further justifying their incorporation into BG matrices for multifunctional orthopedic applications. Table 1 indicates the prospective applications of the dopant materials (bismuth, zinc, and copper) in bioglass and specifies the potential benefits of integrating their oxides.

The synthesized BG in current study was prepared via an acidic sol-gel process, using sodium silicate (NaSiO<sub>3</sub>) and calcium nitrate (Ca(NO<sub>3</sub>)<sub>2</sub>·4H<sub>2</sub>O) as precursors. The sol was subsequently transitioned to a gel, then dried, and calcinated at temperature (700°C). X-ray diffraction (XRD) and Fourier-transform infrared spectroscopy (FTIR) were used to assess the crystalline phase composition and functional group of the doped BG. Furthermore, to evaluate the mechanical behavior and fluid flow within the developed scaffolds under simulated physiological conditions, the study considered the finite element method (FEM) for ANSYS Static Structural and finite volume method (FVM) for fluent simulations respectively. The particular modeling approaches enable a comprehensive assessment of scaffold performance, offering insights into stress distribution and hemodynamic behavior for predicting clinical efficacy in bone tissue engineering. The purpose of the study is to assess the integration of bismuth (Bi), zinc (Zn), and copper (Cu) in the formulation of BG, with the synthesized materials intended for potential use in the regeneration of damaged bone tissue. Addition of dopants such as Bi, Zn, and Cu enhance the localized treatment of bone malignancies, aiming to combine therapeutic effects with enhanced mechanical integrity.

## 2 | Materials and Methods

### 2.1 | Bioglass (BG) Synthesis

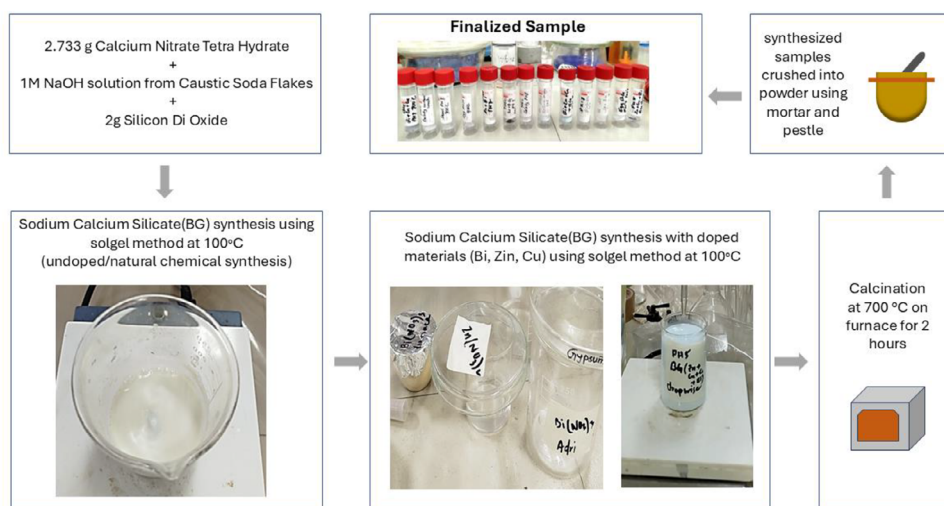
BG was prepared with a composition of 50 mol% SiO<sub>2</sub>, 25 mol% Na<sub>2</sub>O, and 25 mol% CaO [17] using the solgel process. The main precursors were sodium silicate (Na<sub>2</sub>SiO<sub>3</sub>) and calcium nitrate tetrahydrate (Ca(NO<sub>3</sub>)<sub>2</sub>·4H<sub>2</sub>O). By adding 1 M NaOH with 2 g of silicon dioxide, with a 2:1 ratio of silicon dioxide to sodium hydroxide, sodium silicate was developed. Subsequently, a 20 mL calcium nitrate solution of 2.733 g was added to the mixture. The pH of the prepared solution was adjusted to roughly 3 by adding nitric acid (HNO<sub>3</sub>). After approximately 3 h of constant heating over 2 days, the solution soon turned into a gel. After drying in an oven at 100°C for 5 h, this gel developed into a solid and was crushed into a fine powder (Figure 1). To control the pH of the BG between 6 and 8, the BG powder was separated and rinsed with DI water. This sample was dried at 100°C for 45–60 min. Subsequently, the sample underwent calcination at a temperature of 700°C in a furnace for a duration of 2 h, following the methodology used in the study of J.P. Nayak [18] and Rainer et al. [19]. Similar solutions were prepared using snail shell *Gibbula umbilicalis* (95% CaCO<sub>3</sub>) and egg Shell (97% CaCO<sub>3</sub>).

Doped samples were synthesized using 5 g of a 20 mL bismuth nitrate, zinc nitrate, and copper nitrate solution respectively including 4 mL 0.56 M Zn (NO<sub>3</sub>)<sub>2</sub>, 3 mL 0.78 M Bi(NO<sub>3</sub>)<sub>3</sub>, and 3 mL 1.035 M Cu(NO<sub>3</sub>)<sub>2</sub>. BG with doped materials also



**TABLE 1** | Biological implications of dopant incorporation (bismuth, zinc, and copper).

Bismuth	Antibacterial, radiopacity [13]
Zinc	Osteoblast differentiation, antibacterial activity [14]
Copper	Angiogenesis [15], hydroxyapatite formation, antibacterial properties [16]

**FIGURE 1** | Flowchart of the BG synthesis workflow step by step.**TABLE 2** | Molar ratio of all components in the samples.

Sample	SiO <sub>2</sub>	CaO	Na <sub>2</sub> O	Bi <sub>2</sub> O <sub>3</sub>	CuO	ZnO
BG (no doping)	50%	25%	25%	—	—	—
BG (Snail Shell) <i>Gibbula umbilicalis</i> (95% CaCO <sub>3</sub> )	50%	25%	25%	—	—	—
BG (EggShell) (97% CaCO <sub>3</sub> )	50%	25%	25%	—	—	—
BG (doped with Zn(NO <sub>3</sub> ) <sub>2</sub> )	48.90%	24.45%	24.45%	—	—	2.19%
BG (doped with Bi(NO <sub>3</sub> ) <sub>3</sub> )	49.42%	24.71%	24.71%	1.16%	—	—
BG (doped with Cu(NO <sub>3</sub> ) <sub>2</sub> )	48.49%	24.25%	24.25%	—	3.01%	—
BG (doped with Zn(NO <sub>3</sub> ) <sub>2</sub> - Bi(NO <sub>3</sub> ) <sub>3</sub> - Cu(NO <sub>3</sub> ) <sub>2</sub> )	46.942%	23.471%	23.471%	1.098%	2.915%	2.103%

maintained a similar ratio of sodium–calcium–silicate - 50% SiO<sub>2</sub>, 25% Na<sub>2</sub>O, and 25% CaO. Following the incorporation of dopants into the BG mixture, the molar ratio gets modified, as shown in Table 2. The doped samples were similarly rinsed with distilled water balancing each sample to pH 7. Figure 1 outlines the methodologies used during the process, encompassing BG preparation (sol-gel process, drying, calcination, and powder formation). Figure 2 illustrates the methodological steps involved in both the experimental and simulation sections of the study.

## 2.2 | Characterization

The synthesized BG samples were analyzed using a Rigaku SE XRD machine. The powdered samples were subjected to radiation from a ceramic copper tube serving as the radiation source (Cu K $\alpha$ ,  $\lambda$  = 1.54060 Å). The data for the relevant samples were collected, including the intensity (cps) for diffraction angles ranging from  $2\theta$  = (5–700) degrees [20]. The identification of functional groups was conducted by FTIR study within the infrared wavelength range of (280–4000) cm<sup>−1</sup> [21].

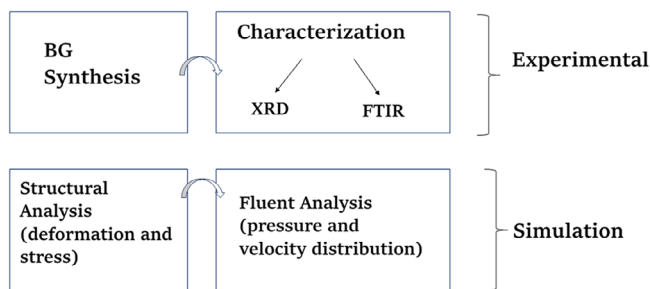


**TABLE 3** | Engineering data of the porous bioglass.

Density	2700 [22]	kg/m <sup>3</sup>
Melting temperature	1070–1278 [23]	°C
Isotropic elasticity	Young's modulus, $E = 16.5$ [24]	GPa
	Poisson's ratio = 0.2692 [24]	—
	Shear modulus, $G = 6.5$ [24]	GPa
	Porosity, $p = 0.52$ [24]	—
Tensile strength	42 [25]	MPa
Compressive strength	~500 [25]	MPa
Tensile ultimate strength	1.2 [24]	GPa
Compressive ultimate strength	0.43 [24]	GPa

**TABLE 4** | Material properties of the fluid (blood).

Density	1060 [20]	kg/m <sup>3</sup>
Specific heat	3620 [26]	J/kg K
Thermal conductivity	0.52 [27]	W/m K
Viscosity	0.003 [27]	kg/m s

**FIGURE 2** | Flowchart of the sequential steps of the study.

### 2.3 | Computational Modeling of the Bioactive Glass Scaffold the Bioactive Glass Scaffold and Surrounding Fluid Domain

*Ansys SpaceClaim* was employed to create a three-dimensional porous (matrix) BG (Figure 3) structure. The tablet version of the permeable BG scaffold had a cylindrical shape, with a radius of 0.5 cm and a height of 10 mm. In this study, we considered a particular geometry of the scaffold with a radius  $R = 8.49$  mm and a height,  $h = 16$  mm along with a microchannel network of diameter  $d = 0.5$  mm (Figure 3) for simplicity of analysis. A fluid domain of dimensions  $40.98 \text{ mm} \times 26.98 \text{ mm} \times 20 \text{ mm}$  (Figure 4) was incorporated surrounding the porous BG body, through which the blood was set to flow. Additionally, a  $4 \times 4$  microchannel network (Figure 5c) was also considered inside the cylindrical BG scaffold. The rationale for this design stems from the fact that the scaffold is often positioned within the bone tissues, and blood flows through channel to support the growth of new cells. Blood flow through the fluid domain, across the scaffold was modeled, and the flow characteristics were examined, considering the properties of fluid (blood), provided in Table 3. ANSYS Static Structural was used to assess the mechanical stability of the BG scaffold within bone

tissue. Following this, engineering reference data for porous BG (see Table 4) and Sodium–Calcium–Silicate (see Table 5) were assembled to simulate the stress distribution and the potential deformation across the scaffold, caused by the applied fluid flow forces.

### 2.4 | Turbulence Model and Boundary Condition

The hemodynamic analysis was a steady state analysis employing Reynold's Averaged Navier Stokes (RANS) model—particularly RANS  $k$ - $\epsilon$  realizable model. Due to the low computational requirements, the model was deemed appropriate for the analyses. Moreover, since the analysis solely focused on flow characteristics and completely disregards any thermal effect, energy equation in the model. The residuals targets were set at  $10^{-5}$  for all 6 (continuity, three-dimensional velocity, turbulence kinetic energy  $k$  and turbulence dissipation rate  $\epsilon$ ) criterion.

**Inlet boundary condition:** The hydraulic diameter for a rectangular duct is defined as  $D_h = \frac{2ab}{a+b}$ , where  $a$  and  $b$  are sides of the duct inlet. For the model of interest, the duct has dimension of  $26.98 \text{ mm} \times 40.98 \text{ mm}$ . Using the equation for hydraulic diameter  $D_h$ , the obtained value was  $3.25 \times 10^{-2} \text{ m}$ . The inlet type was chosen as velocity inlet with a velocity of  $3 \times 10^{-3} \text{ ms}^{-1}$  (Table 6) which is typical flow velocity within an aorta. Although the bio-glass scaffolds are not placed in aortas, it was chosen as the inlet velocity nevertheless as a reference value.

The associated turbulent intensity at the inlet was determined using the following equation:

$$\text{Turbulent intensity, } I = 0.016 (Re_{D_h})^{-\frac{1}{8}}$$



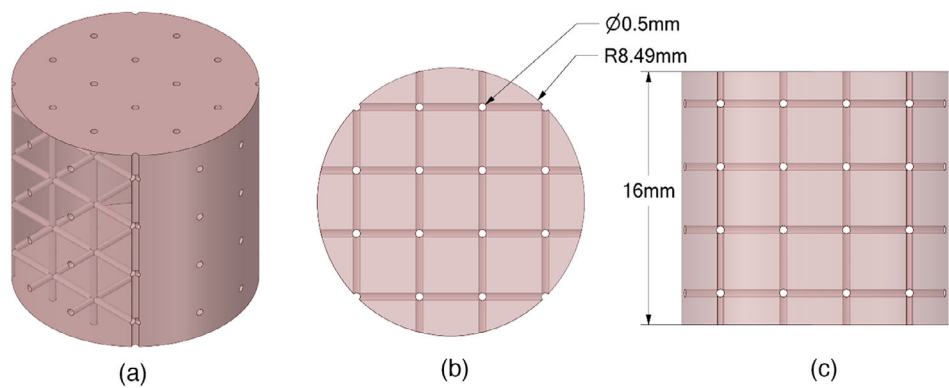


**FIGURE 3** | (a) Isometric view, (b) top view, (c) side view of bioglass (BG) scaffold with microchannel network.

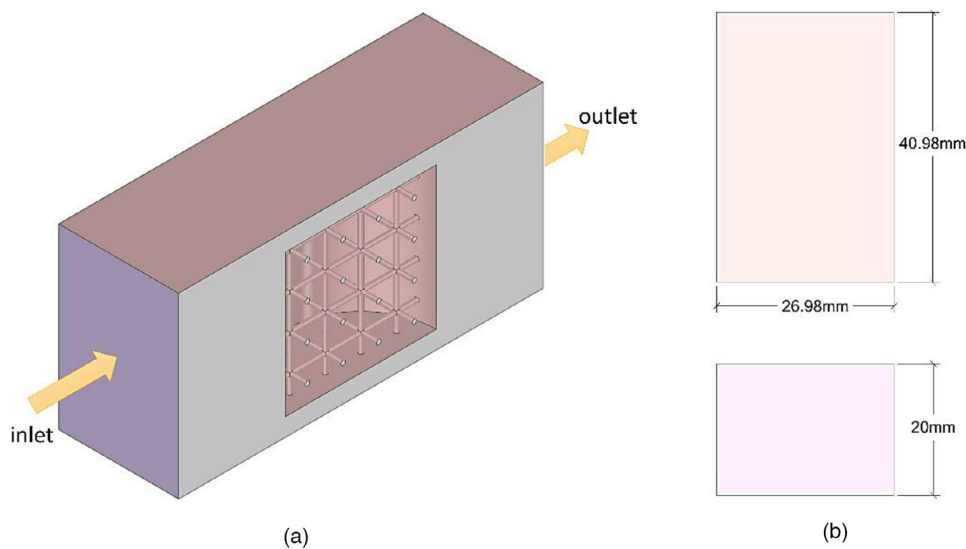


**FIGURE 4** | (a) Cross section view of the fluid domain around the porous bioglass (BG) positioned at the center, and (b) top and front view of the fluid domain.

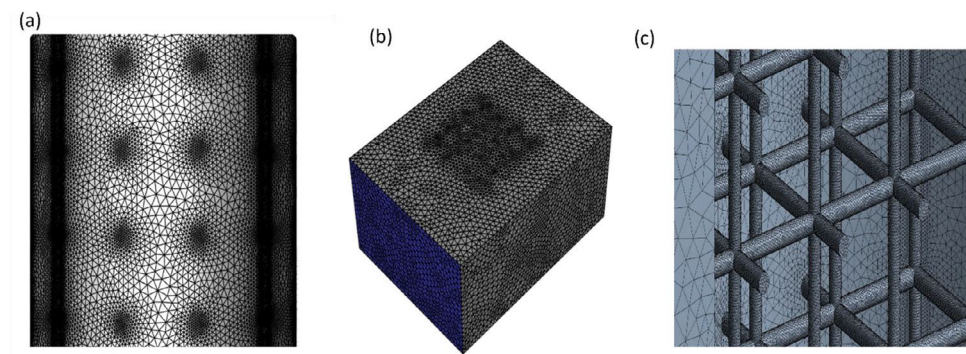


**FIGURE 5** | Mesh generation of the porous bioglass (BG) scaffold: (a) Body of the scaffold, (b) Fluid domain enclosing the scaffold, and (c) Porous matrix within the scaffold structure.

**TABLE 5** | Material properties of the bioglass body (sodium calcium silicate).

Density	2700 [22]	$\text{kg/m}^3$
Specific heat	850 [28]	$\text{J/kg K}$
Thermal conductivity	1.38 [29]	$\text{W/m K}$



**TABLE 6** | Specific boundary conditions considered for CFD simulation.

Inlet	Velocity inlet	$3 \times 10^{-3} \text{ ms}^{-1}$
Outlet	Pressure outlet	Gauge pressure = 0
Wall	No slip condition	—

In which, the Reynold's number were in turn measured by the following equation:

$$\text{Reynold's number, } Re_{DH} = \frac{\rho v D_h}{\nu}$$

For the geometric model of interest, Reynold's number were found 3.445 which lies in the laminar flow region, and the corresponding turbulent intensity was found to be 1.37%.

**Outlet boundary condition:** The outlet was chosen as pressure outlet with a gauge pressure value of 0.

**Wall treatment:** All the walls of the geometry (both the outer walls of the domain and the blood-bioglass interface walls) were set to have no-slip condition as shown in Table 6.

## 2.5 | Mesh Sensitivity Analyses

The complex porous channel system throughout the BG scaffold makes it challenging to generate a structured mesh that is also conformal. Thus, tetrahedral unstructured mesh was chosen as the primary mesh, with prism elements at inflation layer as with such element's conformity is easier to achieve. Among the studied meshes, the cases that are chosen as candidates for mesh sensitivity analyses is shown in Table 7.

From the analyses, it is evident that the surface elements at BG surface needs to be below a particular dimension ( $1 \times 10^{-4} \text{ m}$ ) for the analysis to converge. As for inflation layers on the blood-bioglass interface, while it does not significantly affect the convergence, the flow through pore channels does show variation with higher number of inflation layers and with finer mesh. But regardless of inflation layer height, the velocity drops at the locations where microchannels meet is well captured by all meshes as seen in Figure 6.

Figure 7 illustrates the velocity distribution at the center of the outlet across  $x$  direction. It is evident that only for domain maximum length (which affects the resolution of outlet face). However, as long as the parameter is set below  $1 \times 10^{-3} \text{ m}$ , the distribution coincides with <2% deviation. Considering the time constraints and computational costs, mesh 3 (Table 6) was chosen for the final analysis.

## 3 | Results and Discussions

### 3.1 | XRD Characterization

The crystalline phases of the samples were identified using XRD characterization. Figure 7 presents four distinct diffraction

patterns, each displaying characteristic peaks at specific angles. The potential forms of Sodium Calcium Silicate are highlighted in the graphs using different marks. In the graph captions *Snail PH7* and *Egg PH7* indicate samples of BG containing *Snailshell Gibbula umbilicalis* (95%  $\text{CaCO}_3$ ) and Eggshell (97%  $\text{CaCO}_3$ ), both exhibiting a pH level of 7.

Figure 8a displays the XRD pattern for the materials (Bi-Zn-Cu-BG, Bi-BG, Bi-Zn-BG) that underwent calcination at  $100^\circ\text{C}$ . The predominant peak in the samples is of Devitrite (JCPDS-751252) [30] or sodium calcium silicate ( $\text{Na}_2\text{Ca}_3\text{Si}_6\text{O}_{16}$ ) at an angle of  $2\theta = 29.86^\circ$ . Here, additional peaks were observed at around  $32^\circ$ ,  $38^\circ$ , and  $48^\circ$  for the Bi-Zn-Cu combination. A comparable peak of Devitrite was identified in the study conducted by Yanrui Mao et al., where XRD peaks were observed at  $29^\circ$  and  $36^\circ$  [31]. Rest of the peaks might consist of Combeite ( $\text{Na}_6\text{Ca}_3\text{Si}_6\text{O}_{18}$ ) (JCPDS-751687) [32], similar to prominent peaks found in the study of Pritam et al. which primarily focused on 45S5 bioglass using various acid catalysts [33]. Calcium silicate peaks were also observed at multiple diffraction angles in the research conducted by Pragyan Paramita et al. [14], which are identical to the peaks of Bi-BG and Bi-Zn-BG samples. It could be concluded that the composition might be of Devitrite [34] and Combeite [35] by confirming the peaks at angles ( $32^\circ$ ,  $38^\circ$ , and  $48^\circ$ ).

Figure 8b shows a pronounced diffraction peak at  $29.8^\circ$  for Sodium Calcium Silicate ( $\text{Na}_2\text{Ca}_3\text{Si}_6\text{O}_{16}$ ) in the Bi-Zn-Cu-BG, Bi-BG, and Zn-BG samples respectively (that was calcinated to  $700^\circ\text{C}$ ). The finding is consistent with the study of Elisa Fiume et al., who observed peaks within the range of  $25^\circ$ – $35^\circ$  [36]. The observed minor peaks at  $35^\circ$  and  $38^\circ$  angles, could be attributed to tetrasodium tetracalcium cyclo-hexasilicate ( $\text{Na}_4\text{Ca}_4\text{Si}_6\text{O}_{18}$ ), in agreement with the XRD analysis observed by Luqman et al. [37]. Small peaks of calcium silicate ( $\text{Ca}_6\text{Si}_6\text{O}_{18}$ ) were also identified at angles ranging from  $35^\circ$  to  $42.5^\circ$ , similar to XRD pattern of glass ceramic material studied by Yang Weizhong [38]. Furthermore, an observable peak of Parawollastonite ( $\text{Ca}_{12}\text{Si}_{12}\text{O}_{36}$ ) also identified at  $2\theta = 23^\circ \pm 0.5^\circ$  and  $32^\circ \pm 0.5^\circ$ , respectively [39].

The graph depicted in Figure 8c displays the peak at angle  $2\theta = 30^\circ$  corresponding to Devitrite (JCPDS-23-0671) or tetrasodium tetracalcium cyclo-hexasilicat [40]. The minor peaks of Bi-BG, Snail-BG, and Egg-BG had identical sodium calcium silicate ( $\text{Na}_2\text{Ca}_2\text{Si}_3\text{O}_9$ ) peaks within the range of  $25^\circ$  to  $48^\circ$ , which are identical to doped BG glasses. In addition, Wollastonite (JCPDS-84065) [41] or  $\text{CaSiO}_3$  (JCPDS-00-043-1460) [42] peaks were also observed besides sodium calcium silicate.

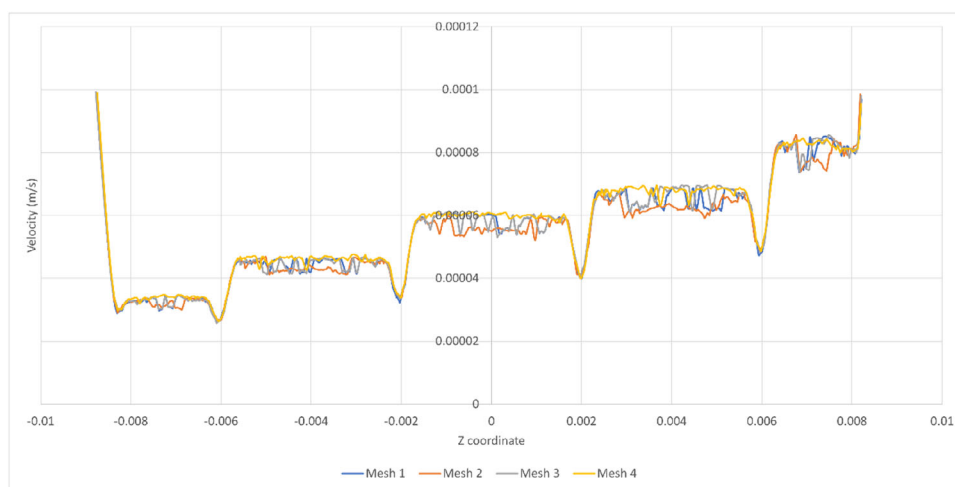
Figure 8d displays XRD patterns of three types of glass: standard bioglass, bioglass derived from Snail shell, and Cu-doped bioactive glass that underwent calcination at  $700^\circ\text{C}$ . The primary



TABLE 7 | Cases considered for mesh sensitivity analysis.

Mesh 1: Unstructured Tetrahedrons + Conformal Mesh (Converges)			
Nodes	1,276,472	Elements	4,609,287
Inflation layers (BG surface) and growth	2 and 1.1	Inflation layer max height (BG surface)	1.00E-04
Inflation layers (Domain wall) and growth	4 and 1.1	Inflation mode (Domain wall)	Smooth transition, 0.272
BG surface face mesh max length	1.00E-04	Domain maximum mesh length	1.00E-03
Mesh 2: Unstructured Tetrahedrons + Conformal Mesh (Does Not Converge)			
Nodes	1,054,326	Elements	3,781,459
Inflation layers (BG surface) and growth	2 and 1.1	Inflation layer max height (BG surface)	1.10E-04
Inflation layers (Domain wall) and growth	4 and 1.1	Inflation mode (Domain wall)	Smooth transition, 0.272
BG surface face mesh max length	1.10E-04	Domain maximum mesh length	1.10E-03
Mesh 3: Unstructured Tetrahedrons + Conformal Mesh (Converges)			
Nodes	1,265,800	Elements	4,558,134
Inflation layers (BG surface) and growth	2 and 1.1	Inflation layer max height (BG surface)	1.00E-04
Inflation layers (Domain wall) and growth	4 and 1.1	Inflation mode (Domain wall)	Smooth transition, 0.272
BG surface face mesh max length	1.00E-04	Domain maximum mesh length	1.10E-03
Mesh 4: Unstructured Tetrahedrons + Conformal Mesh (Converges)			
Nodes	1,022,350	Elements	4,211,256
Inflation layers (BG surface) and growth	1 and 1.1	Inflation layer max height (BG surface)	1.00E-04
Inflation layers (Domain wall) and growth	2 and 1.1	Inflation mode (Domain wall)	Smooth transition, 0.272
BG surface face mesh max length	1.00E-04	Domain maximum mesh length	2.00E-03





**FIGURE 6** | Velocity through a porous microchannel for selected mesh candidates.

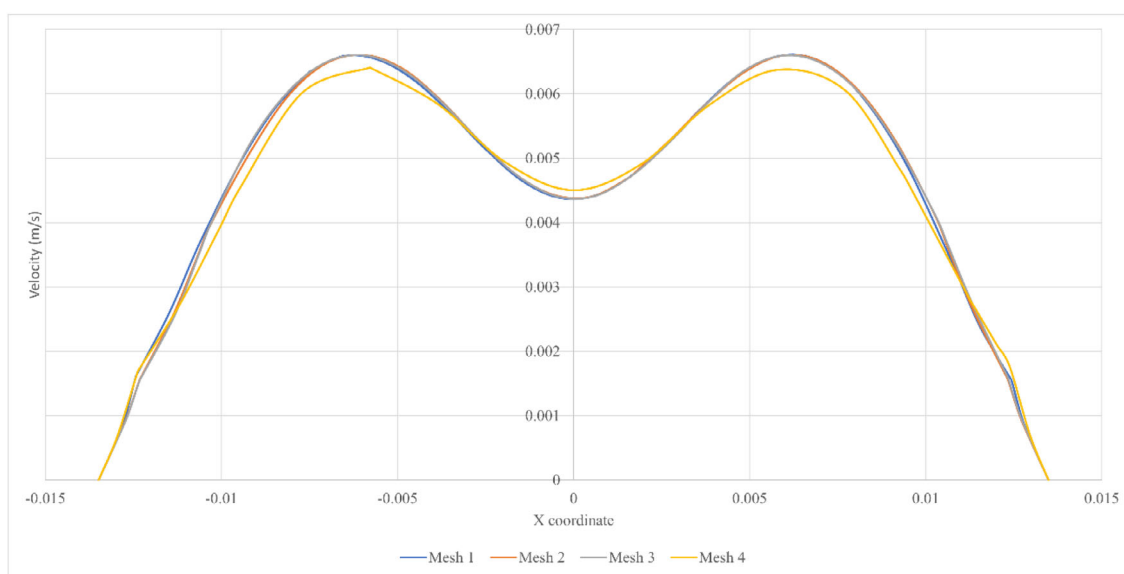


**FIGURE 7** | Velocity distribution at the center of the outlet across  $x$  direction.

**TABLE 8** | FTIR spectra range of BG components.

Functional group	FTIR wavenumber spectrum ( $\text{cm}^{-1}$ )
Si-O-Si	1000–1100
Ca-O	750–1000
$(\text{CO}_3)^{2-}$	1400–1500
H-OH(Hydroxyl)	1500–2000
O-Si-O	800–600

peaks of intensity are evident at  $20^\circ$ ,  $23^\circ$ ,  $26.8^\circ$ ,  $29.8^\circ$ ,  $33^\circ$ ,  $36^\circ$ ,  $39^\circ$ , and  $48.6^\circ$ . The prominent peaks detected correspond to various forms of sodium calcium silicate ( $\text{Na}_4\text{Ca}_4\text{Si}_6\text{O}_{18}$ ,  $\text{Na}_2\text{Ca}_3\text{Si}_6\text{O}_{16}$  and  $\text{Na}_6\text{Ca}_3\text{Si}_6\text{O}_{18}$ ) corroborating by the findings of Pirayesh and Nychka [43], Knowles et al. [44] and Golubevas et al. [45] during BG synthesizing.

Overall, the analysis confirms the presence of Sodium Calcium Silicate as the dominant crystalline phase, present at peak  $2\theta = 29.8^\circ$ . XRD pattern (Figure 8d) also revealed two distinct peaks may be attributed to Devitrite or Combeite. The presence of crystalline phase might be due to grain fractions or phase separation.



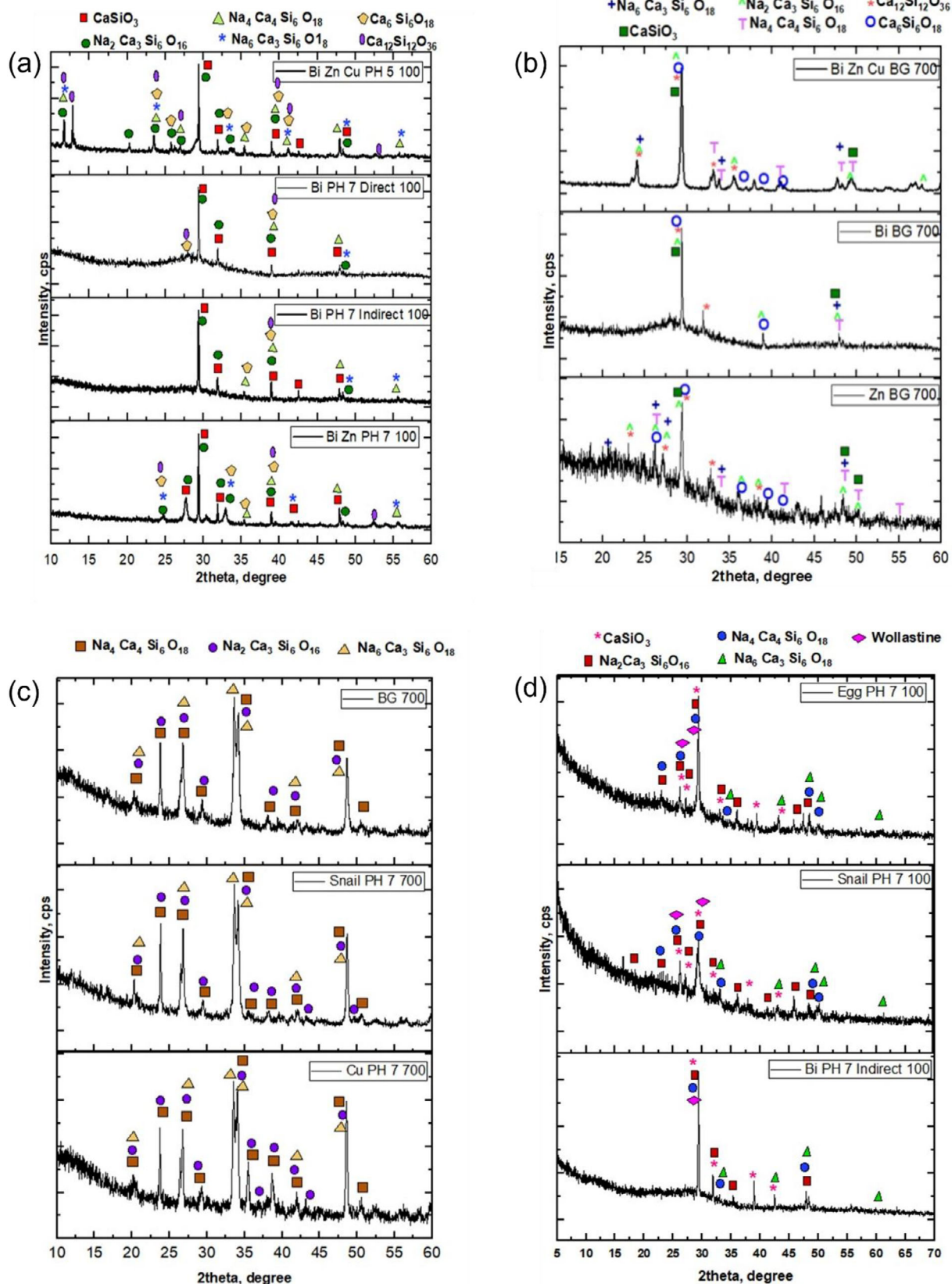


**FIGURE 8** | XRD Characterization (diffraction angle vs. intensity)—(a) Bi-Zn-Cu-BG, Bi-BG, Bi-Zn-BG calcinated at 100°C; (b) Bi-Zn-Cu-BG, Bi-BG, Zn-BG calcinated at 700°C; (c) Eggshell-BG, Snailshell-BG, Bi-BG Calcinated at 100°C; (d) BG, Snailshell-BG, Cu-BG calcinated at 700°C.



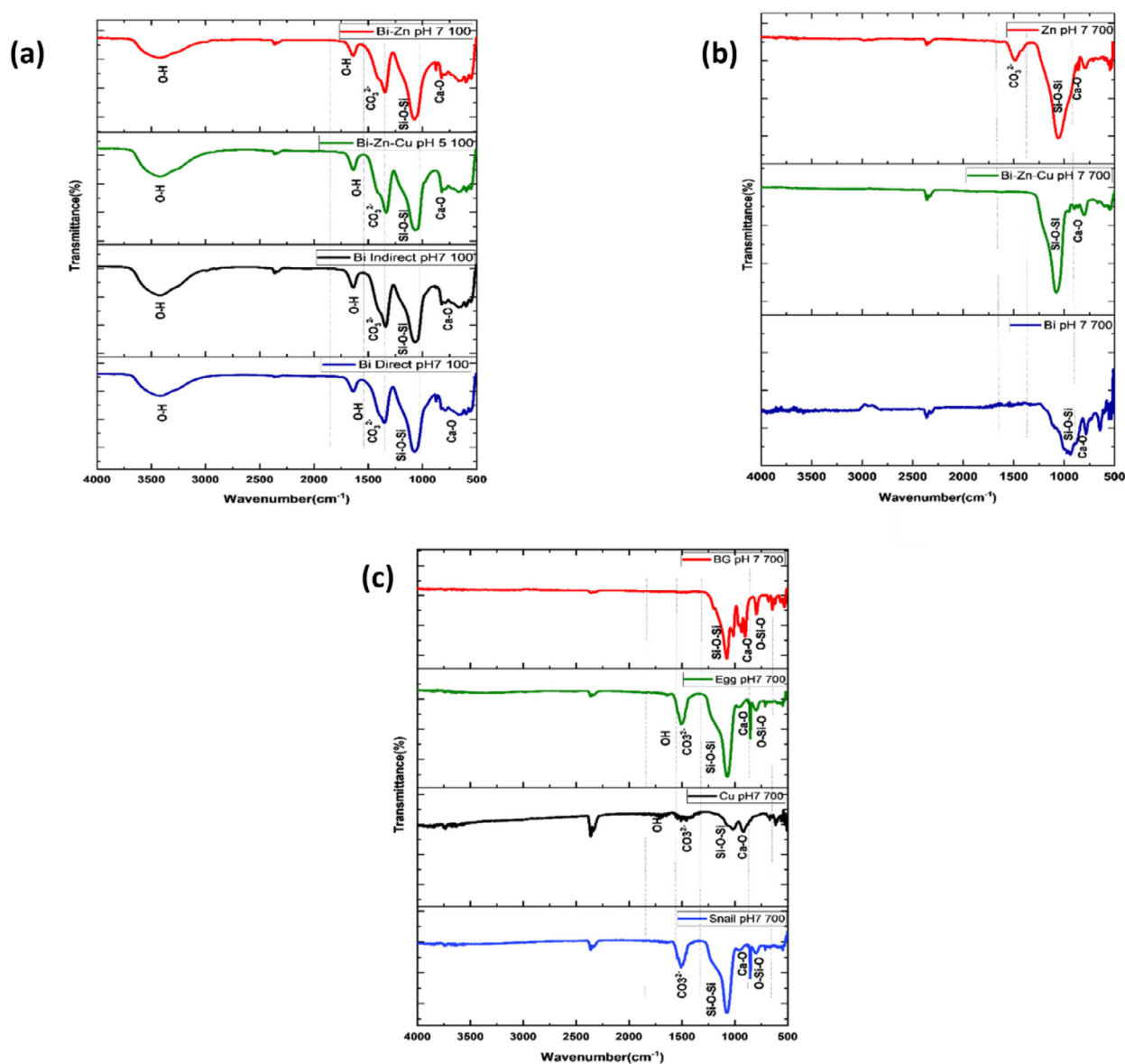


**FIGURE 9** | FTIR analysis (Wavenumber vs Transmittance) (a) Bi-Zn-Cu-BG, Bi-BG, Bi-Zn-BG calcinated at 100°C; (b) Bi-Zn-Cu-BG, Bi-BG, Zn-BG calcinated at 700°C; (c) BG, Eggshell-BG, Snailshell-BG, Cu-BG calcinated at 700°C.

### 3.2 | FTIR Analysis

FTIR was employed in the study the functional group of the synthesized BG with and without dopant. Figure 9 depicts the FTIR spectra of samples calcined at 100°C and 700°C. The majority of the functional groups identified were fundamental functional groups of sodium calcium silicate which are Si-O-Si, CaO, and O-Si-O respectively.

Among the illustrated plots, Figure 9a exhibits the FTIR spectrum of Bi-Zn-Cu-BG, Bi-BG, and Bi-Zn-BG samples calcined at 100°C. The Si-O-Si group peak was detected at 1082 cm<sup>-1</sup> in the FTIR spectra, analogous to the findings of Quintero Sierra L et al. [46] where the transmittance occurred at about 1097 cm<sup>-1</sup>. The functional group of Ca-O was observed at 968 cm<sup>-1</sup> [47], following the Si-O-Si peak. In Figure 9a, the peak of the hydroxyl functional group was observed at 3000–3500 cm<sup>-1</sup> and 1500–2000

cm<sup>-1</sup> respectively, which can be compared with the results of S. Estrada-Flores's study [48]. The presence of hydroxyl in the sample indicated incomplete drying.

The FTIR analysis of Bi-Zn-Cu-BG, Bi-BG, and Zn-BG samples calcined at 700°C was depicted in Figure 9b. The graphs exhibit the absence of the O-H functional group due to calcination. Although, the CO<sub>3</sub><sup>2-</sup> (carbonate) group was identified in the Zn-BG sample at a wavenumber of 1500 cm<sup>-1</sup>, consistent with the findings of S. Estrada-Flores [48]. Subsequently, the Si-O-Si bond displayed the highest peak at 1045 cm<sup>-1</sup>. The Si-O-Si group was visible adjacent to the peak of calcium oxide functional group between 750 and 1000 cm<sup>-1</sup> [49, 50]. It was apparent that the FTIR peak for each functional group varied at different calcination temperatures. The chemical structure of the material altered at elevated temperatures, producing separate peaks for analogous functional groups.



Four samples were depicted in Figure 9c, which include (BG, Eggshell-BG, Snail shell-BG, and Cu-BG) that were calcined at 700°C. The presence of CO<sub>2</sub> in the analysis was a result of the samples remaining in the air for an extended period during the FTIR analysis, which accounts for the presence of CO<sub>3</sub><sup>2-</sup> group peak. The presence Si–O–Si group at 1064 cm<sup>-1</sup>, corresponds to the standard peak. The CaO group may be observable within the transmittance range of 900–1000 cm<sup>-1</sup> [50], with a small peak in each sample. Next to the CaO peak, the O–Si–O group showed a narrow and distinct peak between 800 and 600 cm<sup>-1</sup>, which was also observed by S. Barzgar et al. in their studies [51].

Overall, the FTIR spectra identified the presence of Si–O–Si, CaO, O–Si–O, and occasionally CO<sub>3</sub><sup>2-</sup> and hydroxyl peaks in the FTIR plots. Random carbonate peaks in the graph, suggest that the samples might have been exposed to the natural environment during examination, resulting in a reaction with carbon dioxide. However, the primary functional groups exhibited characteristic peaks in transmittance during the FTIR analysis are given below.

### 3.3 | ANSYS Static Structural Analysis

The structural analysis of the synthesized samples was conducted using ANSYS Static Structural Analysis. Figure 10 illustrates the stress distribution and deformation profiles of the BG. The primary objective of this investigation was to assess the potential structural distortions in BG induced by blood flow. To achieve this, systolic blood pressure values were applied, and the corresponding magnitudes of deformation resulting from this pressure were quantified.

Figure 10a,b illustrate the stress contours on the undoped bioactive glass (BG) body. Pressure was applied to the surfaces of the porous matrix, which was treated as a stationary body. Based on a systolic blood pressure of 60 mm Hg [52] the corresponding applied pressure was approximately 8000 Pa. The tension was applied along the Y-axis. From the data, the average pressure applied was around 5110 Pa.

The contours indicate that the highest stress occurred at the circular faces (inlet and outlet), where the pores were located. Additionally, the cylindrical circumferential area also experienced stress, though it remained within normal limits at approximately 3200 Pa. The greatest stress concentration was observed in the porous region of the BG, where blood flow occurs. However, since the average stress remained below the arterial systolic pressure (threshold of 60 mm Hg), the structural integrity of the bioactive glass had been maintained. This suggested that the BG design is suitable for implantation in fractured bones.

Figure 10c,d shows the total deformation contour of the porous BG structure. Notable distortion was visible near the outlet and along the circumferential region of the glass. The maximum deformation observed along the eight edges was found to be  $2.86 \times 10^{-10}$  m, indicating minimal displacement. Some variation in deformation was also noted along the pores of the outlet. While the inner surfaces of the pores showed no significant distortion, the edges of the pores experienced slight deformation ranging 1.58–0.635 Å. Deformation in the outer circumferential region also varied slightly, within a narrow range of 0–0.12 Å.

The pores in the circumferential region, like those at the inlet and outlet, did not exhibit central distortion. However, a slight increase in deformation was observed as the pore radius increased. Minor distortion was also seen at the four corners of the BG. Nonetheless, the overall magnitude of deformation—given it was measured in angstroms—was negligible. Thus, the structure was found to be sufficiently robust to support application in joints or fractured bone sites, as the deformation was too small for blood flow to cause disruption.

### 3.4 | ANSYS CFD Fluent Analysis

#### 3.4.1 | Pressure Profile

Figure 11 displays seven pressure contour profiles of the fluid domain encircling the undoped BG body, using ANSYS fluent simulations. These profiles depict the distribution of pressure values at different positions on the BG surface and the outlet. The associated pressure gradients (Pa) are illustrated in the adjacent chart with the seven contour plots. The contours illustrate pressure distributions at the inlet (11a), outlet (11b), and at cross-sectional points  $x = -0.005$  (11c),  $x = 0.001$  (11d),  $x = 0.004$  (11e),  $x = 0.01$  (11f), and  $x = 0.02$  (11g), respectively.

Figure 11 illustrates a gradual decrease observed in pressure, as the fluid (blood) moves toward the outlet. At the inlet, the pressure was approximately 0.732 Pa (Figure 11a), which steadily declined to around 0.0067 Pa at the outlet (Figure 11b). Pressure variations are evident at different locations throughout the domain. In the X-axis, the negative sign represents pressure directed toward the inlet, while the positive sign indicates flow toward the outlet. Figure 11c–g illustrates the transition that was visible in pressure magnitudes, indicating a gradual shift toward lower values. As the flow approached the outlet, the contours progressively shifted from orange to blue, signifying a decline in pressure.

The emphasis on depicting the pressure profile aimed to assess the risk factors associated with elevated pressure around the edges and corners of the BG structure. A separation was discernible near the porous matrix since it contained a total of 16 rod-shaped matrices within the body, as illustrated in Figure 5c. In the porous matrix region, particularly around  $x = 0.01$  m, the pressure ranges between 0.421 and 0.067 Pa. This reduction confirmed that the porous structure imposes a flow constraint, contributing to the observed pressure drop. Above all, the pressure seemed to be suitable for the BG's incorporation within the bones, comparing it with the regular blood pressure level.

#### 3.4.2 | Velocity Profile

The velocity profile was evaluated using ANSYS Fluent 2020 R1, where the inlet velocity was considered as the representative of blood flow ( $3 \times 10^{-3}$  m/s) [53]. The magnitudes of the velocity gradients were noted as the flow advanced toward the BG. Seven velocity contour plots were plotted for the identical locations employed in the pressure contour analysis (Figure 12).

Figure 12a shows the initial velocity at the fluid box inlet, measured to be approximately  $3 \times 10^{-3}$  m/s [53], which was



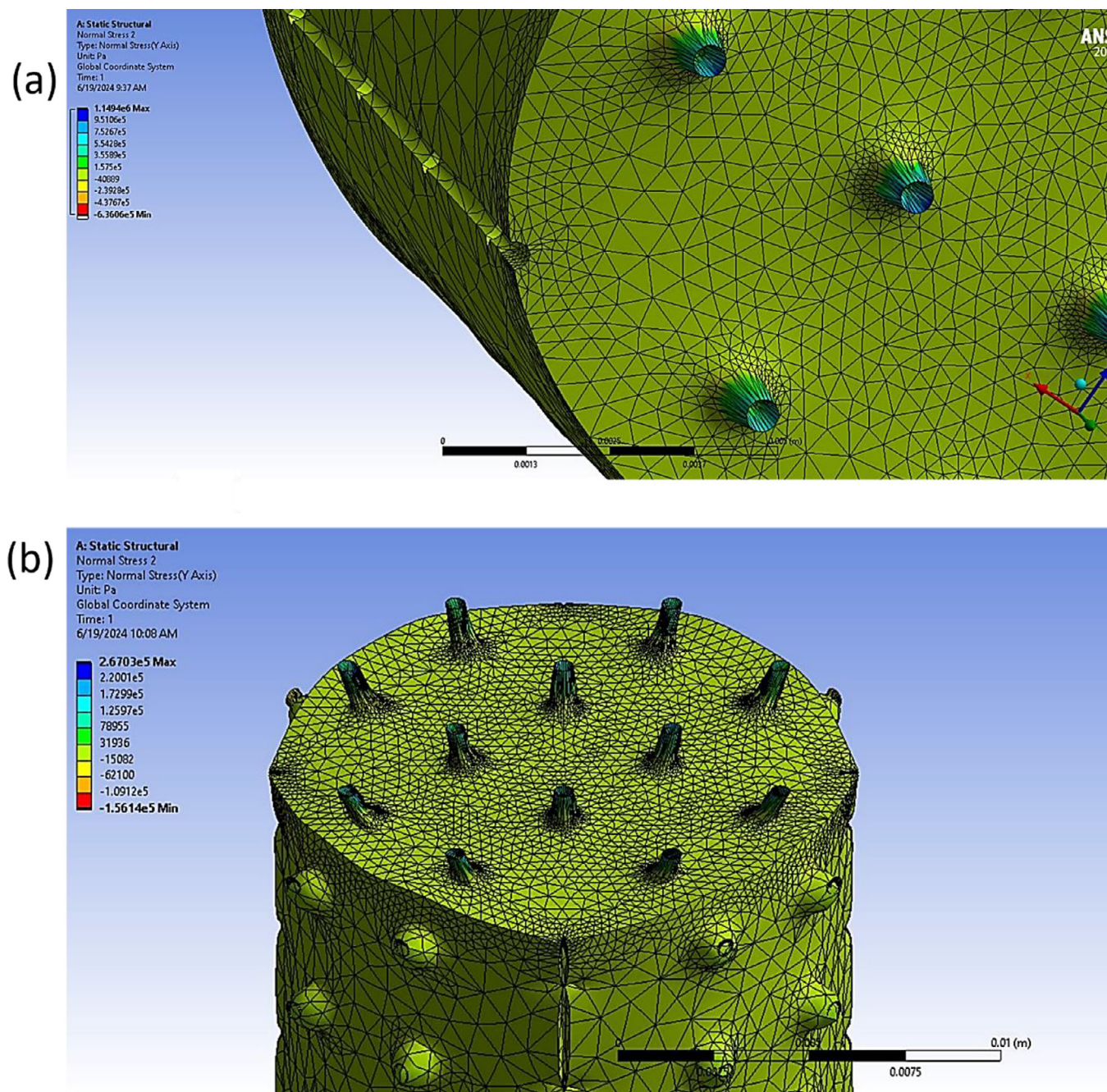


**FIGURE 10** | Structural analysis of the porous bioglass (BG): (a) stress distribution along the  $-Y$  axis (outlet), (b) stress distribution at the edges, (c) total deformation contour along the  $-Y$  axis (outlet), and (d) total deformation at the edges.

consistent with typical blood flow velocity in the aorta. At the outlet (Figure 12b), the velocity contour patterns exhibited variations, but the flow remained steady across the scaffold region, as indicated by uniform contour outlines.

The velocity peaked at  $3.46 \times 10^{-2}$  m/s at positions  $x = \pm 0.02$  m (Figure 12g), which corresponded to the lateral boundaries of the scaffold. These results suggested that blood flow remained stable as it approached the porous matrix, minimizing the risk of stress-induced damage to the glass structure.

With the incorporation of a velocity-based outlet in the boundary conditions, the velocity distribution revealed minimal flow at the inlet of the fluid domain. Conversely, at the exit, two oval-shaped gradients- with varying velocity values could be observed. This occurred due to the cylindrical shape of the BG, which altered the blood flow at the edges, gradually generating friction in the flow. Thus, these separations of fluent velocity were noted at the outflow. Additionally, the porous matrices had minimal impact on the velocity due to their relatively small radius ( $r \sim 0.25$  mm). It caused limited flow



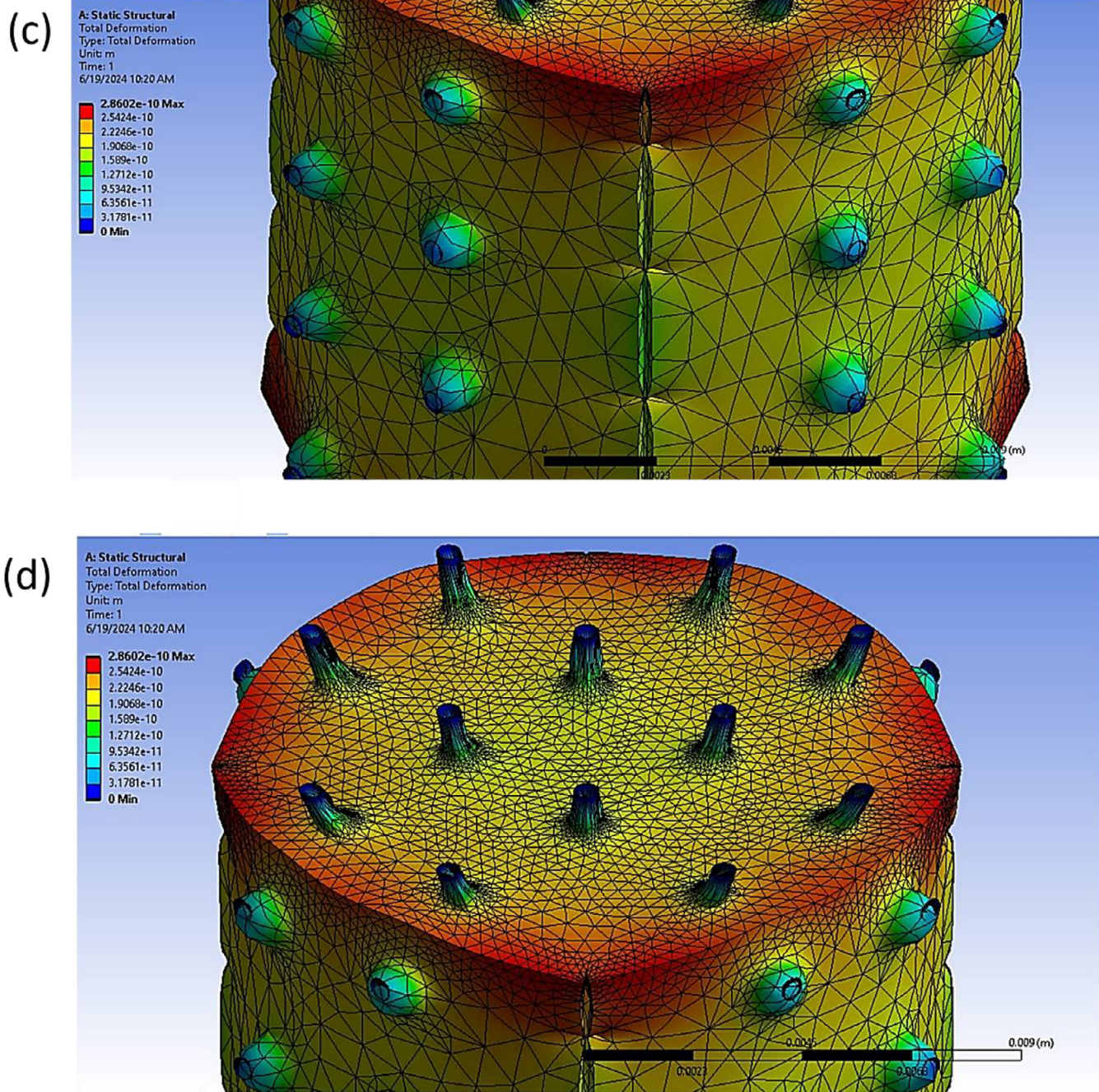


**FIGURE 10** | (Continued)

entry into the holes, which did not significantly alter flow velocity.

This study focused solely on cylindrical geometries for BG scaffold. However, alternative configurations such as (square, oval, rectangular, or capsule-like) shapes may also be imagined for modeling the scaffold. The results presented here provide a foundation for future structural simulations that are critical in shaping the mechanical and functional characteristics of BG scaffolds. The demonstrated role of geometry in influencing

flow behavior highlights the importance of further evaluation of optimized scaffold designs.

In this study, bismuth (Bi), zinc (Zn), and copper (Cu) were incorporated as dopant materials due to their owing to their well-recognized roles in bone regeneration applications. The aim of the study was to incorporate these materials to understand the influence of different molar ratios (shown in Table 2) while doping BG using sol-gel process. The characterization study exclusively examined non-radioactive simulants to avoid potential risk and



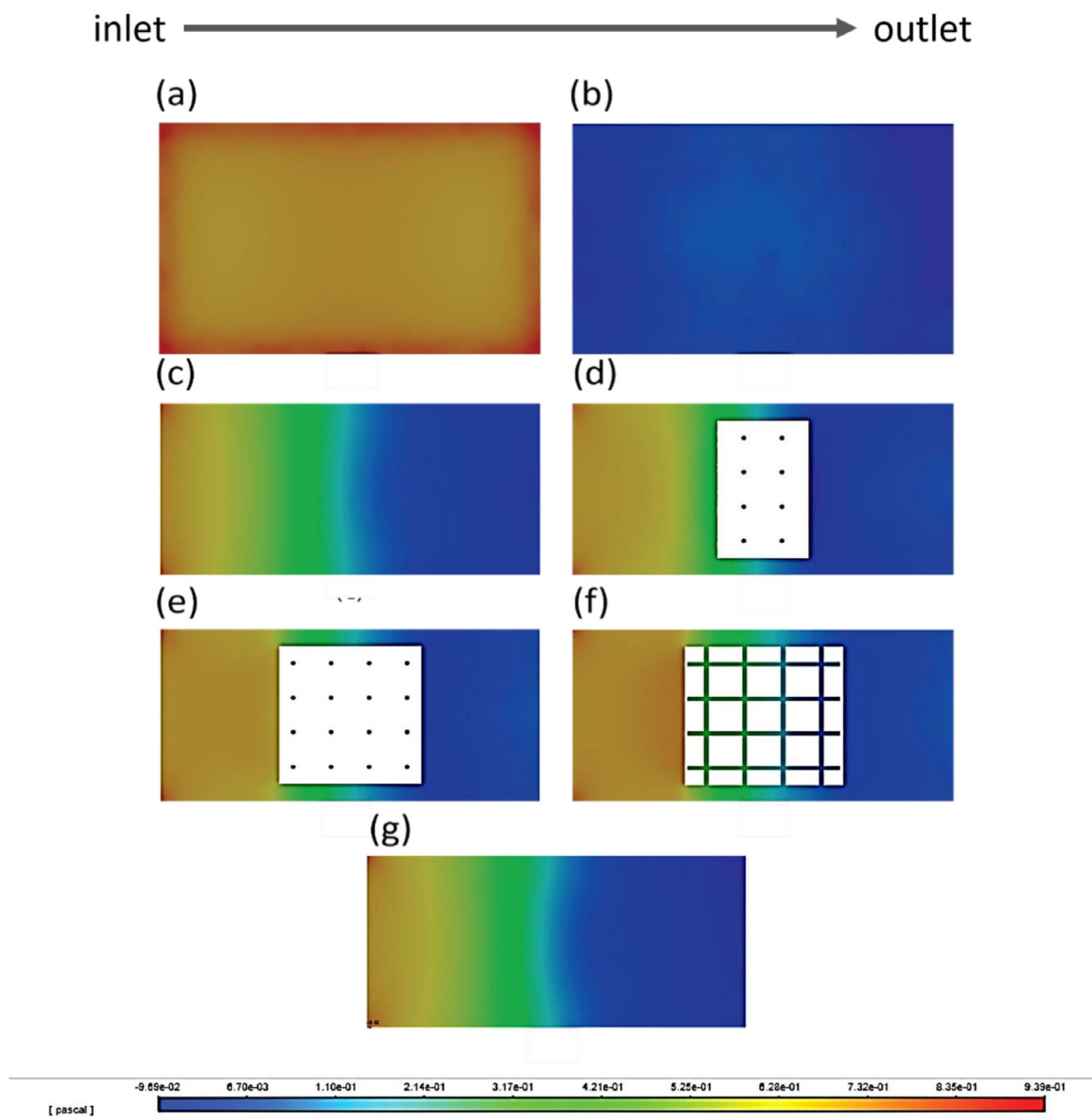


**FIGURE 11** | Pressure profile analysis of fluid box (blood) surrounding the undoped BG body—pressure profile at different positions: (a) Pressure at inlet of the fluid box, (b) Pressure at outlet of the fluid box, (c) Pressure at  $x = -0.005$ , (d) Pressure at  $x = 0.001$ , (e) Pressure at  $x = 0.004$ , (f) Pressure at  $x = 0.01$ , and (g) Pressure at  $x = 0.02$ .

hazards. To build on this work, future studies should generate reliable reference data that clearly differentiate the pressure and velocity profiles between doped and undoped BG systems. Additionally, investigations involving radioactive isotopes of Bi, Zn, and Cu using COMSOL Multiphysics are planned. Extending these simulations to doped porous BG scaffolds will provide greater insights, as the present ANSYS structural analysis was restricted to undoped sodium calcium silicate.

#### 4 | Conclusion

The  $\text{SiO}_2\text{--Na}_2\text{O--CaO}$  bioactive glass doped with Bi, Zn, and Cu was successfully synthesized in this study. Structural analysis of the porous undoped BG model immersed in blood, demonstrated favorable mechanical behavior, including accept-

able levels of stress, deformation, pressure, and velocity. Notably, the maximum stress observed remained below the arterial systolic pressure (60 mm Hg), indicating the material's compatibility with physiological loading conditions. The deformation results showed minimal displacement overall, with slightly elevated deformation at the edges and nearly zero deformation in the inner regions—making the structure suitable for bone implantation.

XRD analysis revealed prominent peaks corresponding to Devitrite at  $2\theta = 29.8^\circ$ , suggesting the formation of sodium calcium silicate ( $\text{Na}_2\text{Ca}_3\text{Si}_6\text{O}_{16}$ ), as well as additional peaks in the range of  $2\theta = 32\text{--}48^\circ$ , which may indicate the presence of Combeite ( $\text{Na}_6\text{Ca}_3\text{Si}_6\text{O}_{18}$ ). FTIR spectroscopy further confirmed the characteristic Silicate (Si–O–Si) bonds, with a strong transmittance peak at  $1082\text{ cm}^{-1}$ .



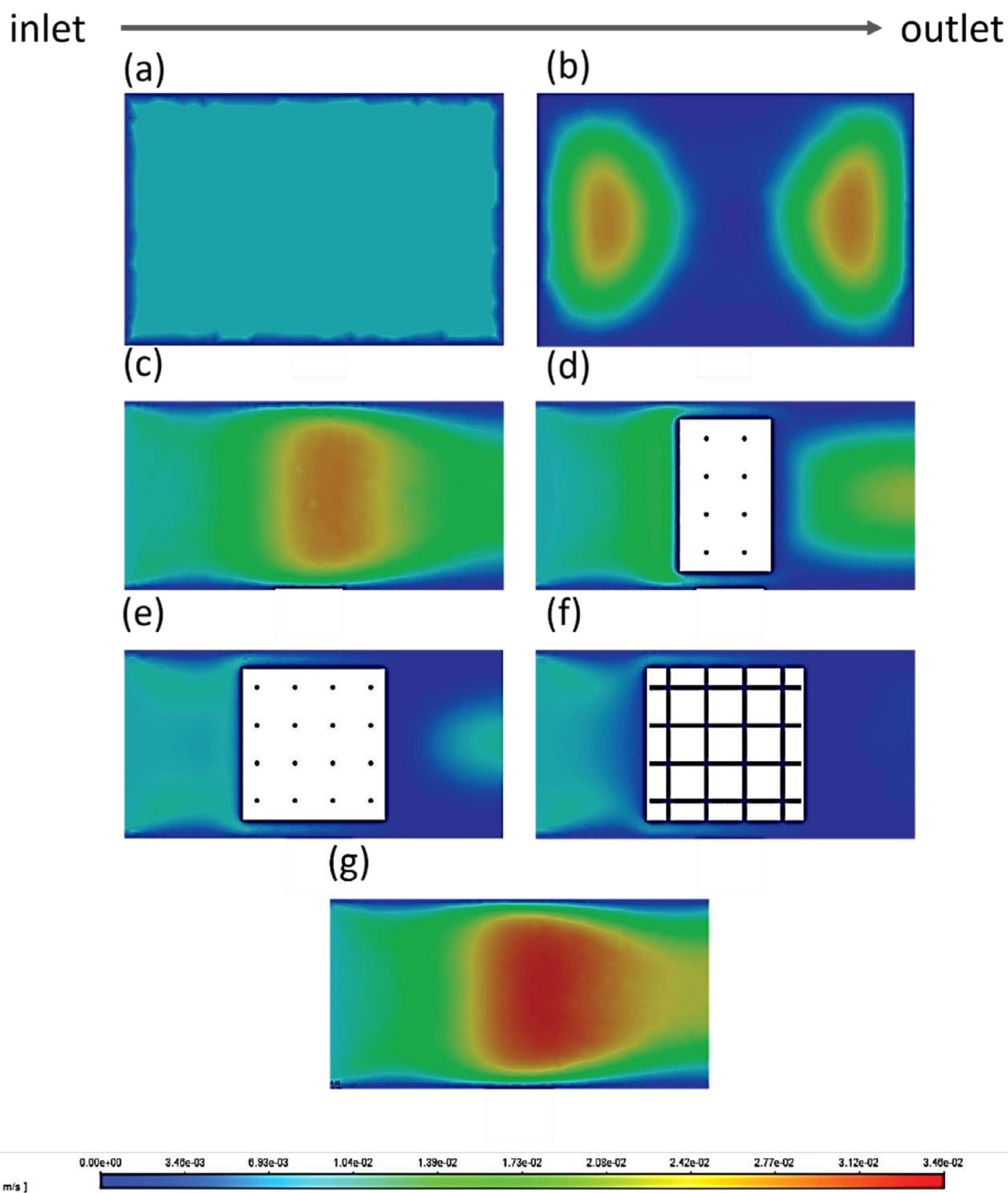


**FIGURE 12** | Velocity profile analysis of fluid box (blood) surrounding the undoped BG body-pressure profile at different positions, (a) Velocity at inlet of the fluid box, (b) Velocity at outlet of the fluid box, (c) Velocity at  $x = -0.005$ , (d) Velocity at  $x = 0.001$ , (e) Velocity at  $x = 0.004$ , (f) Velocity at  $x = 0.01$ , (g) Velocity at  $x = 0.02$ .

The fluent pressure gradient indicated that the flow is restricted within the porous region of the BG, leading to a pressure drop at the outlet of the fluent domain. Additionally, the flow remains nearly stable within the porous section at  $x = 0.01$  m, suggesting a steady and consistent blood flow throughout the BG structure.

Overall, both the structural and spectroscopic analyses validate the successful synthesis of bioactive glass with favorable mechanical and compositional properties, confirming its potential for effective application in bone tissue engineering.

The principal objective of this investigation was to establish a bridge between experimental research and simulation studies on

BG. Given the challenges of directly examining blood flow within bone tissue, this work explored potential insights through flow and structural simulations. One of the main limitations encountered was the restricted research timeframe, which confined the experimental characterization to XRD and FTIR analyses. Future studies will expand this scope to include advanced techniques such as SEM, EDS, and TEM analysis for a more comprehensive assessment of material composition. Furthermore, the present simulations were limited to undoped BG, as engineering data for doped systems were unavailable in existing databases. In subsequent work aim to incorporate engineering data for doped materials, which will allow for improved accuracy and broader applicability of the simulations.



## Acknowledgments

This work was supported by the Institute of Glass and Ceramic Research and Testing, Bangladesh Council of Scientific and Industrial Research (BCSIR), Dhaka, Bangladesh.

## Funding

The authors have nothing to report.

## Conflicts of Interest

The authors declare no conflicts of interest.

## Data Availability Statement

The data that support the findings of this study are available from the corresponding author upon reasonable request.

## References

1. Q. Fu, E. Saiz, M. N. Rahaman, and A. P. Tomsia, "Bioactive Glass Scaffolds for Bone Tissue Engineering: State of the Art and Future Perspectives," *Materials Science and Engineering: C* 31, no. 7 (2011): 1245–1256, <https://doi.org/10.1016/j.msec.2011.04.022>.
2. Q. Z. Chen, I. D. Thompson, and A. R. Boccaccini, "45S5 Bioglass®-Derived Glass–Ceramic Scaffolds for Bone Tissue Engineering," *Biomaterials* 27, no. 11 (2006): 2414–2425, <https://doi.org/10.1016/j.biomaterials.2005.11.025>.
3. L. L. Hench, "The Story of Bioglass®," *Journal of Materials Science: Materials in Medicine* 17 (2006): 967–978, <https://doi.org/10.1007/s10856-006-0432-z>.
4. C. Charlena, Y. W. Sari, and W. Islamia, "Variation of Sintering Temperature in the Synthesis of Fluorapatite From Snail Shells (*Achatina fulica*) Using the Sol-Gel Method," *Indonesian Journal of Pure and Applied Chemistry* 6, no. 3 (2023): 152, <https://doi.org/10.26418/indonesian.v6i3.67697>.
5. J. Du, H. Ding, S. Fu, D. Li, and B. Yu, "Bismuth-Coated 80S15C Bioactive Glass Scaffolds for Photothermal Antitumor Therapy and Bone Regeneration," *Frontiers in Bioengineering and Biotechnology* 10 (2023): 1098923, <https://doi.org/10.3389/fbioe.2022.1098923>.
6. M. A. Kenawy, M. A. A. Ghazala, A. S. El Shinawy, T. M. Tiama, and H. H. El-Bahnasawy, "Investigation of Bismuth Nano-Bioactive Glass Doped Iron Oxide Formation and Structure Properties on Biocompatibility," *Europe PMC* (2023), <https://doi.org/10.21203/rs.3.rs-2609480/v1>.
7. M. M. Farag, W. M. Abd-Allah, and H. Y. A. Ahmed, "Study of the Dual Effect of Gamma Irradiation and Strontium Substitution on Bioactivity, Cytotoxicity, and Antimicrobial Properties of 45S5 Bioglass," *Journal of Biomedical Materials Research* 105 (2017): 1646–1655, <https://doi.org/10.1002/jbm.a.36035>.
8. M. Wojasiński, J. Latocha, P. Liszewska, Ł. Makowski, P. Sobieszuk, and T. Ciach, "Scaled-Up 3D-Printed Reactor for Precipitation of Lecithin-Modified Hydroxyapatite Nanoparticles," *Industrial & Engineering Chemistry Research* 60, no. 35 (2021): 12944–12955, [10.1021/acs.iecr.1c02973](https://doi.org/10.1021/acs.iecr.1c02973).
9. E. Marcello, R. Nigmatullin, P. Basnett, et al., "3D Melt-Extrusion Printing of Medium Chain Length Polyhydroxyalkanoates and Their Application as Antibiotic-Free Antibacterial Scaffolds for Bone Regeneration," *ACS Biomaterials Science & Engineering* 10 (2024): 5136–5153, <https://doi.org/10.1021/acsbiomaterials.4c00624>.
10. V. Sikavitsas, S. Walden, R. Gan, R. Harrison, and D. Papavassiliou, "Biomaterial and Computational Based Strategies for the In Vitro Development of Bone Tissue and Tumor Engineered Constructs" (Dissertation Stephenson School of Biomedical Engineering, The University of Oklahoma), 2017.
11. O. O. Krasnovskaya, D. Abramchuck, A. Erofeev, et al., "Recent Advances in  $^{64}\text{Cu}/^{67}\text{Cu}$ -Based Radiopharmaceuticals," *International Journal of Molecular Sciences* 24, no. 11 (2023): 9154, <https://doi.org/10.3390/ijms24119154>.
12. B. Doty, N. Solomey, J. Folkerts, et al., "Gamma Ray Detection Efficiency of GAGG Crystal Scintillator Using Three Tagged Gamma Ray Techniques," *Nuclear Instruments and Methods in Physics Research Section A: Accelerators, Spectrometers, Detectors and Associated Equipment* 1072 (2024): 170121, <https://arxiv.org/abs/2405.04659>.
13. G. A. Clavijo-Mejía, M. Michálek, M. Arango-Ospina, et al., "Biocompatibility and Antibacterial Activity of Radiopaque Bismuth-Containing Bioactive Glasses," *Ceramics International* 51 (2025): 42725–42733, <https://doi.org/10.1016/j.ceramint.2025.07.016>.
14. P. Paramita, M. Ramachandran, S. Narashiman, et al., "Sol–Gel Based Synthesis and Biological Properties of Zinc Integrated Nano Bioglass Ceramics for Bone Tissue Regeneration," *Journal of Materials Science, Materials in Medicine* 32, no. 1 (2021): 5, <https://doi.org/10.1007/s10856-020-06478-3>.
15. S. N. Rath, A. Brandl, D. Hiller, et al., "Bioactive Copper-Doped Glass Scaffolds Can Stimulate Endothelial Cells in Co-Culture in Combination With Mesenchymal Stem Cells," *PLOS ONE* 9, no. 12 (2014): e113319, <https://doi.org/10.1371/journal.pone.0113319>.
16. F. Bairo, "Copper-Doped Ordered Mesoporous Bioactive Glass: A Promising Multifunctional Platform for Bone Tissue Engineering," *Bioengineering* 7, no. 2 (2020): 45, <https://doi.org/10.3390/bioengineering7020045>.
17. S. Fujibayashi, M. Neo, H. M. Kim, T. Kokubo, and T. Nakamura, "A Comparative Study Between In Vivo Bone Ingrowth and In Vitro Apatite Formation on  $\text{Na}_2\text{O}$ – $\text{CaO}$ – $\text{SiO}_2$  Glasses," *Biomaterials* 24 (2003): 1349–1356, [https://doi.org/10.1016/S0142-9612\(02\)00511-2](https://doi.org/10.1016/S0142-9612(02)00511-2).
18. J. P. Nayak, S. Kumar, and J. Bera, "Sol-Gel Synthesis of Bioglass-Ceramics Using Rice Husk Ash as a Source for Silica and Its Characterization," *Journal of Non-Crystalline Solids* 356, no. 28–30 (2010): 1447–1451, <https://doi.org/10.1016/j.jnoncrysol.2010.04.041>.
19. A. Rainer, S. M. Giannitelli, F. Abbruzzese, E. Traversa, S. Licoccia, and M. Trombetta, "Fabrication of Bioactive Glass-Ceramic Foams Mimicking Human Bone Portions for Regenerative Medicine," *Acta Biomaterialia* 4 (2007): 362–369, <https://doi.org/10.1016/j.actbio.2007.08.007>.
20. M. Kawsar, M. Sahadat Hossain, S. Tabassum, N. M. Bahadur, and S. Ahmed, "Different Solvents and Organic Modifiers for the Control of Crystallographic Parameters in Nano-Crystallite Hydroxyapatite for Amplification of Photocatalytic Activity," *Nanoscale Advances* 6, no. 10 (2024): 2682–2700, <https://doi.org/10.1039/d3na01122d>.
21. N. A. Zarifah, K. A. Matori, H. A. A. Sidek, et al., "Effect of Hydroxyapatite Reinforced With 45S5 Glass on Physical, Structural and Mechanical Properties," *Procedia Chemistry* 19 (2016): 30–37, <https://doi.org/10.1016/j.proche.2016.03.008>.
22. L. de Siqueira, L. Grenho, M. H. Fernandes, F. J. Monteiro, and E. S. Trichês, "45S5 Bioglass-Derived Glass-Ceramic Scaffolds Containing Niobium Obtained by Gelcasting Method," *Materials Research* 24, no. 1 (2021), <https://doi.org/10.1590/1980-5373-MR-2020-0403>.
23. D. Bellucci, V. Cannillo, and A. Sola, "An Overview of the Effects of Thermal Processing on Bioactive Glasses," *Science of Sintering* 42, no. 3 (2010): 307–320, <https://doi.org/10.2298/SOS1003307B>.
24. F. Bairo and E. Fiume, "Elastic Mechanical Properties of 45S5-Based Bioactive Glass-Ceramic Scaffolds," *Materials* 12, no. 19 (2019): 3244, <https://doi.org/10.3390/ma12193244>.
25. M. N. Uddin, P. S. Dhanasekaran, and R. Asmatulu, "Synthesis, Characterization, and Applications of Polymer Based Biomaterials," *Advance in Nanotechnology* 22 (2019): 143–182.
26. Y.-M. Chu, U. Khan, A. Shafiq, and A. Zaib, "Numerical Simulations of Time-Dependent Micro-Rotation Blood Flow Induced by a Curved Moving Surface Through Conduction of Gold Particles with Non-uniform



- Heat Sink/Source,” *Arabian Journal for Science and Engineering* 46, no. 3 (2021): 2413–2427, <https://doi.org/10.1007/s13369-020-05106-0>.
27. P. J. Rodríguez de Rivera, M. Rodríguez de Rivera, F. Socorro, J. A. L. Calbet, and M. Rodríguez de Rivera, “Advantages of In Vivo Measurement of Human Skin Thermal Conductance Using a Calorimetric Sensor,” *Journal of Thermal Analysis and Calorimetry* 147, no. 18 (2022): 10027–10036, <https://doi.org/10.1007/s10973-022-11275-x>.
28. K. Hutkai and D. Katunský, “Insulation of Historic Buildings and Case Study Simulation,” *IOP Conference Series: Materials Science and Engineering* 1209, no. 1 (2021): 012003, <https://doi.org/10.1088/1757-899x/1209/1/012003>.
29. Z. Staliulionis, Z. Zhang, R. Pittini, M. A. E. Andersen, A. Noreika, and P. Tarvydas, “Thermal Modelling and Design of On-Board DC-DC Power Converter Using Finite Element Method,” *Elektronika Ir Elektrotechnika* 20, no. 7 (2014): 38–44, <https://doi.org/10.5755/joi.eee.20.7.8022>.
30. M. H. M. Zaid, K. A. Matori, S. H. A. Aziz, Z. A. Wahab, and S. S. A. Rashid, “Effect of Sintering on Crystallization and Structural Properties of Soda Lime Silica Glass,” *Science of Sintering* 49, no. 4 (2017): 409–417, <https://doi.org/10.2298/SOSI704409>.
31. Y. Mao, J. Liao, M. Wu, et al., “Preparation of Nano Spherical Bioglass by Alkali-Catalyzed Mixed Template,” *Materials Research Express* 7, no. 10 (2020): 105202, <https://doi.org/10.1088/2053-1591/abc373>.
32. Deepali and M. Jayasimhadri, “Structural and Photoluminescence Features of Thermally Stable Red-Emitting Pr<sup>3+</sup>-Doped Sodium Calcium Metasilicate Phosphor for wLED Applications,” *Bulletin of Materials Science* 46, 230 (2023), <https://doi.org/10.1007/s12034-023-03071-6>.
33. P. K. Chakraborty, J. Adhikari, and P. Saha, “Variation of the Properties of Sol-Gel Synthesized Bioactive Glass 45S5 in Organic and Inorganic Acid Catalysts,” *Mater Adv* 2, no. 1 (2021): 413–425, <https://doi.org/10.1039/d0ma00628a>.
34. M. V. Maximov, O. C. Maximov, L. Motelica, et al., “Comprehensive Evaluation of 45S5 Bioactive Glass Doped With Samarium: From Synthesis and Physical Properties to Biocompatibility and Antimicrobial Activity,” *Coatings* 15, no. 4 (2025): 404, <https://doi.org/10.3390/coatings15040404>.
35. L. A. Adams, E. R. Essien, A. T. Adesalu, and M. L. Julius, “Bioactive Glass 45S5 From Diatom Biosilica,” *Journal of Science: Advanced Materials and Devices* 2, no. 4 (2017): 476–482, <https://doi.org/10.1016/j.jsamd.2017.09.002>.
36. E. Fiume, G. Serino, C. Bignardi, E. Verné, and F. Baino, “Sintering Behavior of a Six-Oxide Silicate Bioactive Glass for Scaffold Manufacturing,” *Applied Sciences (Switzerland)* 10, no. 22 (2020): 1–15, <https://doi.org/10.3390/app10228279>.
37. L. A. Adams, E. R. Essien, R. O. Shaibu, and A. Oki, “Sol-Gel Synthesis of SiO<sub>2</sub>-CaO-Na<sub>2</sub>O-P<sub>2</sub>O<sub>5</sub> Bioactive Glass Ceramic From Sodium Metasilicate,” *New Journal of Glass and Ceramics* 3 (2013): 11–15, <https://doi.org/10.4236/njgc.2013.31003>.
38. T. S. R. Ito, *Proceedings of the Japan Academy* 45 (1969): 913–918.
39. Y. Weizhong, C. Zhou, X. Bin, and Z. Dali, “Bioactivity of Sol-Gel Derived Apatite/Wollastonite Porous Bioactive Glass-Ceramic,” *Chinese Journal of Tissue Engineering Research* 10, no. 9 (2006): 185–187.
40. L. A. Adams and E. R. Essien, “In Vitro Transformation of Sol-Gel Derived Bioactive Glass From Sand,” *American Journal of Biomedical Science* 7, no. 4 (2015): 218–228, <https://doi.org/10.5099/aj150400218>.
41. L. A. Núñez-Rodríguez, M. A. Encinas-Romero, A. Gómez-Álvarez, J. L. Valenzuela-García, and G. C. Tiburcio-Munive, “Evaluation of Bioactive Properties of  $\alpha$  and  $\beta$  Wollastonite Bioceramics Soaked in a Simulated Body Fluid,” *Journal of Biomaterials and Nanobiotechnology* 9 (2018): 263–276.
42. R. Lakshmi, V. Velmurugan, and S. Sasikumar, “Preparation and Phase Evolution of Wollastonite by Sol-Gel Combustion Method Using Sucrose as the Fuel,” *Combustion Science and Technology* 185, no. 12 (2013): 1777–1785, <https://doi.org/10.1080/00102202.2013.835308>.
43. H. Pirayesh and J. A. Nychka, “Sol-Gel Synthesis of Bioactive Glass-Ceramic 45S5 and Its In Vitro Dissolution and Mineralization Behavior,” *Journal of the American Ceramic Society* 96 (2013): 1643–1650, <https://doi.org/10.1111/jace.12190>.
44. K. M. Knowles, B. Li, C. N. F. Ramsey, and R. P. Thompson, “Microstructural Characterisation of Devitrite, Na<sub>2</sub>Ca<sub>3</sub>Si<sub>6</sub>O<sub>16</sub>,” *Advanced Materials Research* 585 (2012): 51–55, <https://doi.org/10.4028/www.scientific.net/AMR.585.51>.
45. R. Golubevas, A. Zarkov, L. Alinauskas, et al., “Fabrication and Investigation of High-Quality Glass-Ceramic (GC)-Polymethyl Methacrylate (PMMA) Composite for Regenerative Medicine,” *RSC Advances* 7, no. 53 (2017): 33558–33567, <https://doi.org/10.1039/c7ra05188c>.
46. L. A. Quintero Sierra and D. M. Escobar, “Characterization and Bioactivity Behavior of Sol-Gel Derived Bioactive Vitroceramic From Non-Conventional Precursors,” *Boletín de la Sociedad Española de Cerámica y Vidrio* 58, no. 2 (2019): 85–92, <https://doi.org/10.1016/j.bsecv.2018.07.003>.
47. R. Choudhary, S. Koppala, and S. Swamiappan, “Bioactivity Studies of Calcium Magnesium Silicate Prepared From Eggshell Waste by Sol-Gel Combustion Synthesis,” *Journal of Asian Ceramic Societies* 3, no. 2 (2015): 173–177, <https://doi.org/10.1016/j.jascers.2015.01.002>.
48. S. Estrada-Flores, A. Martínez-Luévano, P. Bartolo-Pérez, L. A. García-Cerda, T. E. Flores-Guía, and E. N. Aguilera-González, “Facile Synthesis of Novel Calcium Silicate Hydrated-Nylon 6/66 Nanocomposites by Solution Mixing Method,” *RSC Advances* 8, no. 73 (2018): 41818–41827, <https://doi.org/10.1039/c8ra07116k>.
49. R. Ellerbrock, M. Stein, and J. Schaller, “Comparing Amorphous Silica, Short-Range-Ordered Silicates and Silicic Acid Species by FTIR,” *Scientific Reports* 12, no. 1 (2022): 11708, <https://doi.org/10.1038/s41598-022-15882-4>.
50. S. Husain, N. H. Haryanti, S. Suryajaya, and A. Permatia, “Synthesis and Characterization of Calcium Silicate From Rice Husk Ash and Snail Shell,” *Jurnal Neutrino* 11, no. 2 (2019): 45, <https://doi.org/10.18860/neu.v11i2.6608>.
51. S. Barzgar, Y. Yan, M. Tarik, J. Skibsted, C. Ludwig, and B. Lothenbach, “A Long-Term Study on Structural Changes in Calcium Aluminate Silicate Hydrates,” *Materials and Structures/Materiaux et Constructions* 55, no. 10 (2022): 243, <https://doi.org/10.1617/s11527-022-02080-x>.
52. “Systolic Blood Pressure—An Overview | ScienceDirect Topics.” Aug. 13, 2024. [Online]. <https://www.sciencedirect.com/topics/medicine-and-dentistry/systolic-blood-pressure>.
53. D. Sidebotham and I. J. Le Grice, “Physiology and Pathophysiology,” *Cardiothoracic Critical Care* (2007): 3–27, <https://doi.org/10.1016/B978-075067572-7.50004-7>.